Ocean Engineering 359 (2026) 125919

Contents lists available at ScienceDirect

Ocean Engineering

journal homepage: www.elsevier.com/locate/oceaneng

Research paper

Deep physics for deep seas: Estimating underwater vehicle dynamics with PINNs

Mirco Vangi *, Alessandro Bucci, Gherardo Liverani, Davide Colasanto, Alessandro Ridolfi, Benedetto Allotta

Department of Industrial Engineering, University of Florence, via di Santa Marta 3, 50139, Florence, Italy
Interuniversity Center of Integrated Systems for the Marine Environment (ISME), Italy[1]

ARTICLE INFO

Keywords:
Autonomous underwater reconfigurable vehicle
Model identification
Dynamic parameter estimation
PINN
Feedforward control system

ABSTRACT

The RUVIFIST (Reconfigurable Underwater Vehicle for Inspection, Free-floating Intervention, and Survey Tasks) platform was developed to combine the long-range endurance of AUVs with the precision and manoeuvrability of ROVs. Its reconfigurable design enables both a streamlined "survey" mode and a compact "hovering" mode for inspection and intervention. The main contribution of this paper is the development of a Physics-Informed Neural Network (PINN) to estimate key hydrodynamic parameters, including added mass and linear damping coefficients, directly from field data, improving the accuracy of the vehicle's dynamic model and enabling a feedforward controller alongside PID control. Experiments focused on estimating surge, sway, and yaw parameters. Performance was assessed by comparing the feedforward control effort with that of a baseline PID controller. In the "survey" configuration, the method achieved high accuracy, with force discrepancies below 5 N during constant-speed surge and below 2 N during heading rotations. In the "hovering" configuration, the estimations remained reliable, with the feedforward controller alone achieving velocity errors of about 0.03 m/s during constant-speed surge and sway motions.

1. Introduction

The RUVIFIST project aimed to develop an underwater vehicle that can incorporate both the Autonomous Underwater Vehicles (AUVs) and Remotely Operated Vehicles (ROVs) functionalities. For instance, the AUV capability of long navigation surveys and the ROV capability of performing a close inspection (or intervention) task. Fig. 1 synthetically summarizes the **R**econfigurable **U**nderwater **V**ehicle for **I**nspection, **F**ree-floating, **I**ntervention and **S**urvey **T**asks (RUVIFIST) concept.

The basic idea concerns a vehicle provided with many configurations and the ability to autonomously switch between them depending on the current task to accomplish. In particular, different robot configurations lead to a different overall vehicle hydrodynamic force and added mass contribution. In particular the Autonomous Underwater Reconfigurable Vehicle (AURV) can actively switch between a configuration with an isotropic behaviour ideal to face intervention operations, named "hovering/opened" (Fig. 2(b)), and an elongated body that minimizes the hydrodynamic drag in the longitudinal direction, minimizing the power consumption, ideal to perform long survey tasks, named "survey/closed" (Fig. 2(a)). It is worth noting that the word "hovering" is introduced to highlight that in the opened configuration, the vehicle is provided with all the six Degree Of Freedoms (DOFs), while, in the "survey" configuration, the vehicle loses the ability to move in the lateral direction of motion (i.e. cannot move along the sway direction).

Since the dynamics of the two extreme configurations differ considerably due to variations in mass distribution, an accurate control strategy is essential to ensure consistent and reliable performance. A Gain Scheduling (GS)-PID control architecture has been previously implemented on the vehicle and presented in Vangi et al. (2025). Nevertheless, adopting a model-based control approach has the potential to further enhance the overall performance of the system. To implement such a controller, it is first necessary to perform a system identification process.

System identification constitutes a fundamental step in the modelling and control of dynamic systems, as it enables the derivation of mathematical representations of the system dynamics. These models are crucial for predicting the behaviour of underwater vehicles and for designing robust and effective control strategies capable of operating reliably in the harsh marine environment. Adopting a model-based control approach has the potential to significantly enhance the overall performance of autonomous systems, as it allows the controller to

* Corresponding author at: Department of Industrial Engineering, University of Florence, via di Santa Marta 3, 50139, Florence, Italy
E-mail address: mirco.vangi@unifi.it (M. Vangi).
[1] www.isme.unige.it

https://doi.org/10.1016/j.oceaneng.2026.125919
Received 11 December 2025; Received in revised form 21 April 2026; Accepted 3 May 2026
Available online 9 May 2026

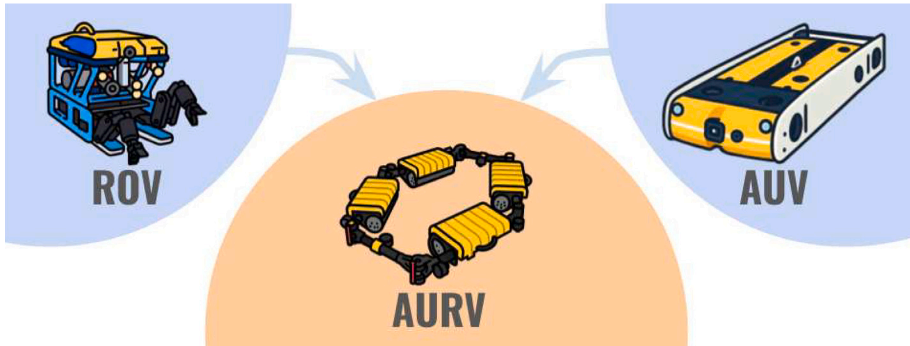

Fig. 1. The RUVIFIST vehicle concept.

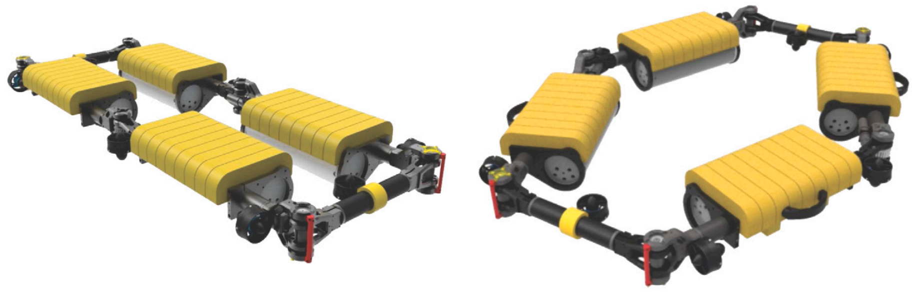

(a) (b)

Fig. 2. The RUVIFIST vehicle in its two extreme configurations. In (a) the "survey" configuration while in (b) the "hovering" configuration.

anticipate necessary actions rather than simply reacting to errors. For example in Chen et al. (2025), a performance-optimized control framework is established for USV-UAV heterogeneous systems to navigate the complexities of 3D sea–air environments. The authors explicitly address the challenge of uncertain dynamics by integrating Prescribed Performance Control (PPC) and Optimal Control methods.

Traditional methodologies for system identification can generally be classified into two main categories: physics-based modelling and purely data-driven approaches. Physics-based methods rely on the governing physical laws of hydrodynamics and rigid-body mechanics to formulate analytical models. While these approaches provide interpretable structures and preserve physical consistency, they often suffer from parameter estimation errors, unmodelled dynamics, and high computational complexity. Conversely, data-driven models exploit only measured data, typically bypassing explicit physical formulations. Although attractive due to their flexibility, these models tend to lack robustness and generalization when applied outside the training domain.

Based on these considerations, we chose to combine data-driven and physics-based approaches by implementing a system identification procedure based on Physics-Informed Neural Networks (PINNs). PINNs are a class of Neural Network (NN) that integrate the governing physical laws of a system into the learning process, effectively combining physics-based knowledge with data-driven modelling. Unlike standard Deep Learning (DL) techniques, PINNs incorporate the system's governing equations directly into the loss function, allowing the model to learn from relatively small datasets while ensuring that the predictions remain physically consistent.

The main contribution of this paper lies in the development and experimental validation of a PINN-based framework for the identification of the hydrodynamic parameters of the RUVIFIST vehicle. Unlike traditional identification approaches, the proposed method embeds the nonlinear underwater vehicle dynamics directly into the loss function, enabling the simultaneous estimation of added mass and linear damping coefficients from field data collected under closed-loop conditions. Furthermore, the identified model is validated through the implementation of a FeedForward (FF) controller and its integration within a GS-PID control architecture. In addition, a first numerical comparison of the dynamic parameters in the two extreme configurations is provided, demonstrating from a mathematical standpoint the main advantages associated with each configuration.

The present work is organized to reflect the natural workflow followed by the authors. In Section 2, a detailed review of the state of the art in system identification, both PINN-based and conventional, is presented. Section 3 describes the system model and the problem formulation; at the end of the section, the implementation of a simple FF control system used to validate the parameter estimation is also presented. Section 4 reports the results of the dynamic parameter estimation performed using the PINN introduced previously. Finally, Section 5 summarizes the main conclusions of this work and outlines potential directions for future research.

2. State of the art

The identification of a dynamic system is a fundamental process in which a mathematical model is derived from experimental input–output data by minimizing a performance criterion (Vincenzi and Gambarelli, 2017; Gambarelli et al., 2014). Typically, this criterion is expressed as a cost function that quantifies the discrepancy between the measured system outputs and those generated by the model. Solving this parameter estimation problem is inherently an optimization task. For simple linear models, analytical solutions may exist. A notable example is the Least Squares (LS) estimator, which minimizes the sum of squared residuals and serves as an optimal unbiased linear estimator under specific statistical assumptions (Rao Sripada and Grant Fisher, 1987). However, when the dynamics are governed by nonlinear differential equations, as is the case for most underwater vehicles, closed-form solutions are generally unattainable. In such scenarios, numerical optimization techniques must be employed to iteratively refine the model parameters. This shift to numerical approaches introduces additional challenges. In particular, the ill-posed nature of inverse problems may lead to non-uniqueness of solutions and the presence of multiple local minima in the cost function landscape (Gori et al., 1992). Addressing these challenges requires careful selection of optimization strategies. Traditional gradient-based methods (Kelley, 1962) provide efficiency for well-posed problems, while more advanced meta-heuristic and Machine Learning (ML) techniques have been proposed to navigate the complex, non-convex search spaces encountered in nonlinear identification (Ramirez et al., 2021). Ultimately, the choice of algorithm has a direct impact on the quality of the identified model, influencing not only its ability to fit the experimental data but also its capacity to generalize to new, previously unobserved system behaviours.

The inherent nonlinearities and strong coupling among different DOFs of underwater vehicles further complicate the identification process. A classical approach to mitigate this complexity is to linearize the nonlinear equations of motion around specific operating points. Identification experiments are then conducted by exciting one DOF at a time, thereby simplifying the parameter estimation procedure. However, this decoupled approach is often insufficient to capture the full nonlinear dynamics, particularly when hydrodynamic interactions across DOFs play a significant role (Thothadri et al., 2003; Martinelli et al., 2024).

In Studt et al. (2022), for example, this methodology was applied to estimate the dynamic parameters of a ballbot. The authors collected a set of uncorrelated input/output measurements and identified parameters from the linearized equations by solving structured linear systems. These estimates were subsequently used as initial guesses for nonlinear parameter identification, thereby improving the robustness of the procedure. Similarly, in Lee et al. (2023), the authors modelled a differential-drive mobile robot as an AutoRegressive–Moving-Average (ARMA) system. By carefully selecting the excitation inputs to ensure full system-mode activation, they applied standard identification algorithms to construct an approximate model from the measured trajectories. These examples highlight the common reliance on linearization and decoupled excitation strategies, which, although effective for certain robotic platforms, remain limited in capturing the nonlinear and strongly coupled hydrodynamics of underwater vehicles.

Most of the physical laws that govern the dynamics of a system can be described by Partial Differential Equations (PDEs). Recently, solving the governing PDEs of physical phenomena using DL has emerged as a new field of scientific machine learning, leveraging the universal approximation theorem and high expressivity of NNs (Hornik et al., 1989; Raissi et al., 2017). In general, Deep Neural Networks (DNNs) could approximate any high-dimensional function given that sufficient training data are supplied (Arzani and Dawson, 2021). Recent advancements in computational power have facilitated the application of ML and DL techniques in system identification, including in the underwater domain Bucci et al. (2020) and Topini and Ridolfi (2025). In Nguyen et al. (2022), a NN framework was employed in a two-phase procedure: first, to perform system identification of the plant, and second, to utilize the identified model in a Model Predictive Control (MPC) scheme for trajectory tracking. These results demonstrated the potential of NN-based methods to bridge the gap between modelling and control design.

Nevertheless, parameter estimation for underwater vehicles is typically conducted under closed-loop conditions, primarily for safety reasons. In such cases, the measured input signals are inherently correlated with noisy output signals, leading to biased estimates when naïve least-squares methods are applied (Van den Hof, 1998; Ljung and Forssell, 1999). A standard remedy is to restrict the input/output datasets to reduce correlation. However, this conflicts with the requirements of data-driven models, such as NN, which rely on large datasets to achieve accurate estimation.

Low data availability for some engineering problems limits the robustness of conventional ML models used for these applications (Raissi et al., 2019). The incorporation of prior knowledge of fundamental physical laws into the training of NNs serves as a regularization mechanism, constraining the space of admissible solutions and enhancing the generalizability of the function approximation. By embedding this prior information into the network, the effective information content of the available data is enriched, enabling the learning algorithm to converge towards the correct solution even in a low data scenario (Bihlo and Popovych, 2022). PINNs have shown robust generalization across various domains, including fluid dynamics (Cai et al., 2021) and electromagnetism (Khan and Lowther, 2022).

In the field of robotic control, recent advances have been achieved through the use of PINNs. For instance, Nicodemus et al. (2022) introduced a PINN-based Nonlinear Model Predictive Control (NMPC) framework for multi-link manipulators, where the PINN acts as a surrogate model of the system dynamics. By embedding the governing differential equations directly into the training loss, the network learns the underlying physics from limited data while enabling efficient gradient computation through automatic differentiation. This approach facilitates real-time control by replacing computationally expensive numerical integrations with fast neural evaluations, achieving substantial speed-ups without compromising control accuracy. The study demonstrates that PINN-based surrogate models can effectively bridge the gap between data-driven modelling and physics-based control in complex mechanical systems. Liu et al. (2024) advance the use of PINN for robotic modelling and control a Franka Emika Panda robot. The results shows that the proposed PINN-based models achieve superior predictive accuracy and robustness compared to black-box methods, effectively linking data-driven learning with model-based control.

In the field of autonomous vehicle control, Gu et al. (2024) propose a PINN framework for accurate and interpretable quadrotor dynamic modelling (Gu et al., 2024). Addressing the limitations of both model-based and purely data-driven approaches, the authors embed the law of conservation of momentum into the loss function as a soft physical constraint, ensuring physically consistent learning. The network serves as an inverse dynamics model, predicting motor inputs from system states and accelerations. Results show that the proposed PINN significantly outperforms linearized models and conventional DL methods in terms of generalization, accuracy, and physical consistency, even when trained on limited data.

In the context of marine robotics, PINNs have been successfully employed to identify hydrodynamic parameters. For instance, in Mishra et al. (2024), PINNs were used to estimate the dynamic coefficients associated with the heave motion of an underwater vehicle, achieving coefficient estimation errors on the order of 10^{-2} in terms of Mean Squared Error (MSE). The dynamic model of an Unmanned Surface Vehicle (USV) was identified using a PINN-based framework. Comparisons against conventional NNs revealed superior performance of PINNs, particularly in predicting sway, surge, and yaw dynamics under limited training data (only 4000 samples) (Xu et al., 2022). These findings indicate that PINNs not only reduce data requirements but also offer enhanced generalization capabilities, suggesting their potential as a viable alternative to conventional DL techniques for underwater vehicle system identification.

3. Materials and methods

3.1. Problem formulation

In the context of this work we follow the underwater vehicle dynamics model presented in (Fossen and Sagatun, 1991; Antonelli and Antonelli, 2014):

$$M\dot{\boldsymbol{\nu}} + C(\boldsymbol{\nu})\boldsymbol{\nu} + D(\boldsymbol{\nu})\boldsymbol{\nu} + \mathbf{g}(\boldsymbol{\eta}) = \boldsymbol{\tau} \tag{1}$$

where:

M = mass and inertia matrix
$C(\boldsymbol{\nu})$ = matrix of Coriolis and centripetal terms

$D(\boldsymbol{\nu})$ = damping matrix
$\mathbf{g}(\boldsymbol{\eta})$ = vector of gravitational and buoyancy forces and moments
$\boldsymbol{\tau}$ = vector of control inputs

When a rigid body moves through a fluid, it must also account for the additional inertia of the surrounding fluid that is set into motion by the body's movement. The fluid surrounding the body is accelerated along with the body itself, requiring an additional force to achieve this acceleration. As a result, the fluid exerts a reaction force on the body that is equal in magnitude but opposite in direction. This reaction force is known as the added mass contribution, and it significantly affects the dynamics of underwater vehicles, making their motion more complex compared to robots operating in air, where these contributions can generally be neglected (Antonelli and Antonelli, 2014).

We can so distinguish two contribution to the mass and inertia matrix, one related to the rigid-body dynamics (M_{RB}) and one related to the added mass (M_A).

$$M = M_{RB} + M_A \tag{2}$$

Under the assumption that the vehicle has three planes of symmetry, we simplify the structure of the matrices M_{RB} and M_A and approximate them as diagonal:

$$M_{RB} = \mathrm{diag}\left(m,\ m,\ m,\ I_p,\ I_q,\ I_r\right) \tag{3}$$

$$M_A = \mathrm{diag}\left(X_{\dot u},\ Y_{\dot v},\ Z_{\dot w},\ K_{\dot p},\ M_{\dot q},\ N_{\dot r}\right) \tag{4}$$

The added mass coefficients can be theoretically derived exploiting the geometry of the rigid body and, eventually, its symmetry, by applying the strip theory and Computational Fluid Dynamics (CFD) analysis (Lambert et al., 2022). However, these methods typically require significant computational resources and substantial user expertise.

As for the mass and inertia matrix, also for the centripetal and Coriolis matrix can be distinguished two contribution:

$$C(\boldsymbol{\nu}) = C_{RB}(\boldsymbol{\nu}) + C_A(\boldsymbol{\nu}) \tag{5}$$

where C_{RB} includes the rigid body effects, and C_A is related to the motion of the vehicle in the surrounding fluid. Differently form the mass matrix M, that has a unique possible representation, the matrix $C(\boldsymbol{\nu})$ does not have an unique representation.

The viscosity of the fluid also causes the presence of dissipative drag and lift forces on the body. A common simplification is to consider only linear, proportional to the velocity, and quadratic, proportional to squares of the velocity, damping terms and group these terms in a matrix $D(\boldsymbol{\nu})$ such that (Makam et al., 2023):

$$D(\boldsymbol{\nu}) > 0 \quad \forall \boldsymbol{\nu} \in \mathbb{R}^6 \tag{6}$$

Under the same assumption adopted for Eqs. (4) and (3), we simplify the matrix structure by approximating it as diagonal:

$$D(\boldsymbol{\nu}) = D_l + D_q(\boldsymbol{\nu}) \tag{7}$$

$$D_l = \mathrm{diag}\left(D_u,\ D_v,\ D_w,\ D_p,\ D_q,\ D_r\right) \tag{8}$$

$$D_q(\boldsymbol{\nu}) = \mathrm{diag}\left(D_{u|u|}|u|,\ D_{v|v|}|v|,\ D_{w|w|}|w|,\ D_{p|p|}|p|,\ D_{q|q|}|q|,\ D_{r|r|}|r|\right) \tag{9}$$

Moreover, considering that typically an AUV travels at relatively low speed, the quadratic terms of the damping matrix can be neglected, leaving only the linear terms acting on the vehicle. Indeed, linear damping primarily arises from viscous friction and skin friction. At very low speeds, the flow around the vehicle is often laminar, and the drag force is dominated by the shearing stresses in the fluid (Fossen, 1994). For reasons of safety and to preserve the battery life of the batteries installed on this first prototype of the RUVIFIST vehicle, the maximum permitted speed during autonomous operation has been set at 0.5 m/s. With this limit set in the vehicle's control system, the quadratic term of the damping matrix $D(\boldsymbol{\nu})$ can be neglected. By using only the linear terms for the damping matrix we also have an important simplification of the dynamic model since the damping matrix is no more dependent from $\boldsymbol{\nu}$.

$$D(\boldsymbol{\nu}) = D_l = \mathrm{diag}\{D_u,\ D_v,\ D_w,\ D_p,\ D_q,\ D_r\} \tag{10}$$

3.2. Parameter estimation

In the scope of this work, we focus on the estimation of the dynamic parameters of the RUVIFIST underwater vehicle, with particular emphasis on the damping matrix and added mass terms.

For the optimization problem we can define the cost function as:

$$f = \|M\dot{\boldsymbol{\nu}} + C(\boldsymbol{\nu})\boldsymbol{\nu} + D_l\,\boldsymbol{\nu} + \mathbf{g}(\boldsymbol{\eta}) - \boldsymbol{\tau}\|^2 \tag{11}$$

where we have to remember that both M and $C(\boldsymbol{\nu})$ also include the added mass terms. The optimization problem can be so formulated as:

$$\begin{aligned} \min_{M_A,\,D_l} \quad & f(M_{RB}, M_A, C_{RB}, C_A, D_l, \dot{\boldsymbol{\nu}}, \boldsymbol{\nu}, \boldsymbol{\eta}, \boldsymbol{\tau}) \\ \text{s.t.} \quad & M_A \geq 0 \\ & D_l \geq 0 \end{aligned} \tag{12}$$

where we have constrained the added mass matrix M_A and the damping matrix D_l to be positive definite.

The proposed solution combines Long Short-Term Memory (LSTM) layers with Fully Connected (FC) layers, as illustrated in Fig. 3. The purpose of the LSTM layer is to capture the temporal features of the input data, since instantaneous data alone are not sufficient to represent the system parameters we aim to estimate. Following this, two stages of FC linear networks are employed, separated by a *Tanh* activation layer, which introduces nonlinear behaviour into the model.

The proposed network architecture receives as input a time vector, representing the time interval between two consecutive samples, together with the linear and angular velocity vector of the vehicle. The objective of the network is to approximate the underlying system dynamics, such that the network output is $\hat{\boldsymbol{\nu}}$, which corresponds to the estimated linear and angular velocities of the vehicle. In addition to the standard NN weights, the model explicitly incorporates a set of learnable physical parameters associated with the dynamic behaviour of the vehicle. Specifically, these parameters correspond to the elements of the added mass matrix M_A and the linear damping matrix D_l. By defining these physical quantities as network parameter objects, they become trainable entities within the architecture. Consequently, they are updated simultaneously with the NN weights during the back-propagation process.

The physic constraints are involved into the training process through the loss function. In particular the non negative constraints are implemented thanks to the function *softplus*$(\cdot)$ from PyTorch (Paszke et al., 2019). The loss function is composed by two terms: one related to the dynamic model of the vehicle, according to Eq. (11), and the other related to the MSE between the actual and predicted vehicle velocities.

$$J(M_A, D_l) = \left\|\left(M_{RB} + M_A\right)\dot{\boldsymbol{\nu}} + \left(C_{RB}(\boldsymbol{\nu}) + C_A(\boldsymbol{\nu})\right)\boldsymbol{\nu} + D_l\,\boldsymbol{\nu} + \mathbf{g}(\boldsymbol{\eta}) - \boldsymbol{\tau}\right\|^2 + \left\|\hat{\boldsymbol{\nu}} - \boldsymbol{\nu}\right\|^2 \tag{13}$$

It is worth noting that the inputs to the neural network differ from the quantities used in the loss function. The LSTM model receives only time and velocity measurements, as shown in Fig. 3. However, acceleration $\dot{\boldsymbol{\nu}}$ is included in the dataset and explicitly used in the physics-based loss defined in Eq. (11). Therefore, although not part of the network input, $\dot{\boldsymbol{\nu}}$ is essential for evaluating the cost function and enforcing the dynamic consistency required by Eq. (12).

In our case, we decided to estimate only a portion of the vehicle's dynamics, considering only surge, sway, and yaw movements. This decision is motivated by the fact that, during typical AUV missions, these DOFs are the ones dynamically excited by the guidance system. Conversely, it is uncommon to dynamically control the vehicle in roll

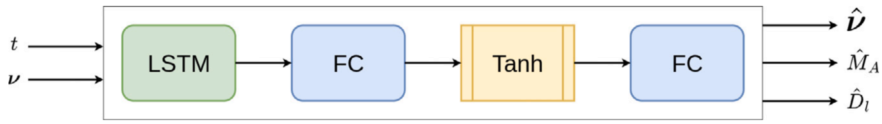

Fig. 3. PINN structure used for parameters estimation.

Table 1
Network parameters.

Layer	Characteristics
LSTM	20 sample time window 5 level deep 1024 hidden size
1st FC linear	1024 input size 512 output size 0.2 dropout
2nd FC linear	512 input size 6 output size 0.2 dropout

and pitch, apart from regulation on desired set-points, usually zero pitch and zero roll.

Different configurations of the PINN layers were tested with the aim of identifying the most accurate model. Since the true parameters of the vehicle are unknown, the estimator was developed and validated using simulated data, which provided known values for the added mass and damping matrices. The results show that the more accurate estimation is performed by a network with the characteristics presented in Table 1.

Algorithm 1 reports the pseudo-code for the estimation process performed with the PINN network.

Algorithm 1: LSTM-PINN Parameter Estimation

Input : Dataset $\mathcal{D} = \{t, \nu, \dot{\nu}, \tau\}$,
Weighting factor α,
Sequence length L

Output: Estimated physical parameters
$\Theta = \{X, Y, I_r, D_x, D_y, D_r\}$

```
Initialize LSTM network 𝓕_ω with weights ω;
Initialize trainable raw parameters Θ_raw;
Pre-process 𝓓 into temporal sequences of length L;
while not converged do
    for each batch 𝓑 ⊂ 𝓓 do
        ν̂ ← 𝓕_ω(𝓑_in) ;        // Forward pass (Prediction)
        Θ ← softplus(Θ_raw) ;    // Ensures physical consistency
        // Physics Residual via Dynamic Model Inversion
        τ_pred ← M(Θ)ν̇ + C(Θ, ν)ν + D(Θ, ν)ν;
        R_physics ← τ_pred − τ;
        // Cost Function Contributions
        𝓛_phys ← mean(‖R_physics‖²);
        𝓛_data ← mean(‖ν̂ − ν‖²);
        𝓛_total ← 𝓛_phys + α 𝓛_data;
        Update (ω, Θ_raw) via Optimizer using ∇𝓛_total;
    Update learning rate via LR scheduler;
return Θ;
```

In Section 4, results for the training and the real experiments are presented. To validate the estimation on the real vehicle, we implemented an onboard FF control system in parallel with the GS-PID controller already implemented on the vehicle. The residual effort of the Proportional Integral Derivative (PID) controller is then used to assess the quality of the estimation: in the case of a perfect estimation, the contribution of the PID should ideally be zero.

It is important to clearly distinguish between the parameter estimation phase and their subsequent deployment. The PINN-based estimation procedure is carried out entirely offline, using data collected under representative operating conditions to accurately identify the model parameters. Once this phase is completed, only the final estimated parameter values are transferred to the vehicle, where they are used online exclusively for the computation of the FF terms. Therefore, the estimation algorithm is not executed in real time on the system, but contributes indirectly to the controller performance through the previously identified parameters.

3.3. Feed-forward control system

A FF control system is the simplest model-based control system that can be implemented to control a system. Generally, in the FF control system, the control signal is obtained by inverting the mathematical model that describes the evolution of the system to be controlled. If we want to control an AUV through a pure FF control system, we can use (1) to describe the system and compute the required $\boldsymbol{\tau}_d$ depending on the desired speed and acceleration of the vehicle $\left[\dot{\boldsymbol{\nu}}_d^T, \boldsymbol{\nu}_d^T, \boldsymbol{\eta}_d^T\right]^T$.

$$\tau_{ff,x} = \hat{X}_{\dot{u}}\ \dot{\nu}_{d,x} + \hat{D}_u\ \nu_{d,x} \tag{14}$$

$$\tau_{ff,y} = \hat{X}_{\dot{v}}\ \dot{\nu}_{d,y} + \hat{D}_v\ \nu_{d,y} \tag{15}$$

$$\tau_{ff,r} = \hat{D}_r\ \nu_{d,r} \tag{16}$$

In a FF system, the control variable adjustment is not error-based but only on knowledge about the process in the form of a mathematical model of the process and knowledge about, or measurements of, the process disturbances. For this reason, generally, the FF control system is supported by a feedback controller (Guzmán et al., 2012; Visioli, 2004) (Fig. 4). A simple solution is to combine FF with PID, in this case, the FF terms allow the system to increase the performance of the PID controller, for example by reducing the rise time (Visioli, 2006).

To accurately compute the FF terms, precise measurement and estimation of the quantities in Eqs. (14)–(16) are required. In underwater robotics, vehicles are typically equipped with multiple navigation sensors capable of measuring linear and angular velocities even underwater where the Global Navigation Satellite System (GNSS) data are neglected. In particular, the RUVIFIST vehicle is equipped with a Doppler Velocity Log (DVL), which provides accurate measurements of the vehicle's linear velocity relative to the seabed, and an Inertial Measurement Unit (IMU), which measures both linear and angular accelerations (Vangi et al., 2025). Accordingly, the terms $\nu_{d,x}$ and $\nu_{d,y}$ are obtained directly from DVL measurements, while $\dot{\nu}_{d,x}$, $\dot{\nu}_{d,y}$, and $\nu_{d,r}$ are derived from IMU data. A detailed list of the navigation devices used on RUVIFIST is presented in Table 2

A FF term acts independently of the feedback loop, meaning it can anticipate the required control action instead of waiting for an error to develop, this results in faster system response and reduces the contribution of the PID controller. Without FF, PID gains often need to be high to achieve acceptable performance. By offloading some of the control effort to FF terms, lower PID gains can be used, reducing potential issues like overshoot and oscillations.

The accuracy of the estimation of the FF action is crucial. If we consider a pure FF controller, an accurate estimation of the parameters

Table 2
Onboard sensors used in the RUVIFIST vehicle.

Sensor	Description	Measuring
KVH DSP 1750	Single-axis Fibre Optic Gyroscope (FOG)	High precision angular velocity along yaw direction
Teledyne Wayfinder DVL	Doppler Velocity Log (DVL)	Linear velocity
Xsens MTi-300	Inertial Measurement Unit (IMU)	Linear and angular acceleration
U-blox 7P	Global Positioning System (GPS)	Position when vehicle is on surface
BlueRobotics Bar30	Depth sensor	High-resolution pressure sensor with 300 m range

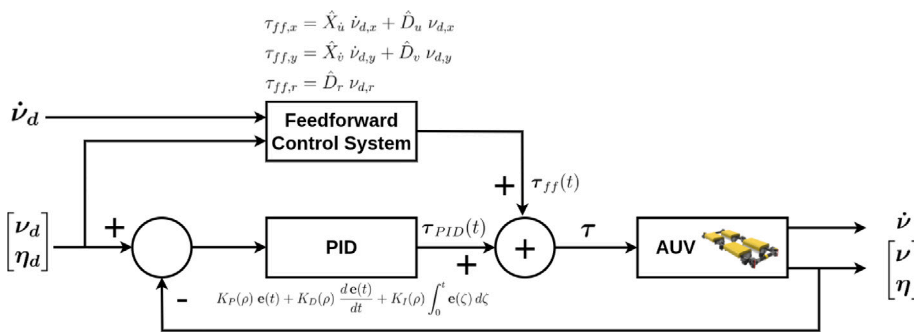

Fig. 4. Feedforward and PID control system scheme.

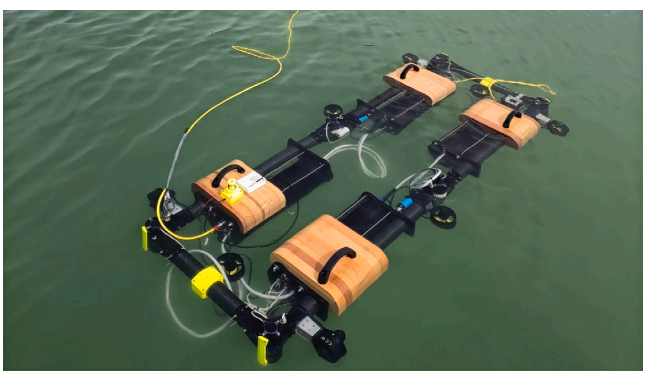

Fig. 5. The RUVIFIST vehicle during the experimental campaign at the Bilancino Lake, Barberino del Mugello (FI), Italy.

will cause a steady-state error that could be not negligible. The PID controller acts alongside the FF controller to correct this error.

A more detailed description of the electromechanical design and the control system implemented on the RUVIFIST vehicle prior to this identification procedure can be found in Vangi et al. (2025).

4. Results

In this chapter we present the results of the parameters estimation approach presented in Section 3 by using data collected during on field campaign performed in Bilancino Lake, Barberino del Mugello (FI), Italy (Fig. 5).

As stated in Section 3.1, only a subset of the vehicle's dynamic parameters—namely surge, sway, and yaw—is considered. This choice is motivated by the observation that, during typical AUV missions, these DOFs are the primary modes dynamically excited by the guidance system. Conversely, roll and pitch are rarely subject to dynamic control and are generally regulated around fixed setpoints, typically corresponding to zero roll and zero pitch.

The training of the NN addresses the optimization problem outlined in Eq. (12). Effective training hinges on a large and representative dataset of the vehicle's operational dynamics. To this end, data were gathered in two separate on-field campaigns. The first campaign collected data for the "survey" configuration by exciting only the surge and yaw DOFs. The second campaign focused on the "hovering" configuration, capturing data across the surge, sway, and yaw DOFs.

Parameter estimation

In "survey" configuration, the data were collected during a mission in which the vehicle performed a small survey inspection along a four-waypoint path. This path was repeated four times at different target speeds: 0.5 m/s, 0.4 m/s, 0.3 m/s, and 0.2 m/s. The target speed profiles were generated using a double-S trajectory with a transient time of 5 s. The resulting vehicle path is shown in Fig. 6.

The mission was executed at a constant depth of 0.6 m over a total distance of just under 400 m, generating approximately 10 500 samples at a frequency of 10 Hz. The raw data were subsequently processed to increase the Signal-To-Noise ration (SNR), particularly for the navigation sensor measurements. The training procedure utilized a Learning Rate (LR) scheduler. During the initial iterations (epochs), the LR was set to a large value to promote rapid convergence towards an optimal set of network weights. In subsequent iterations, the LR was decreased to allow for more precise convergence to the optimal solution. The training results for the estimated parameters (added mass $X_{\dot{u}}$, drag D_u, and drag D_r) are presented in Fig. 7. As shown, the estimates converge rapidly, exhibiting large changes in the initial phase of optimization and only minor fluctuations in the final stages.

It is worth noting that the network does not directly estimate the added mass of the vehicle. Instead, it tries to estimate the sum of the dry mass m and the added mass term M_A. This approach was chosen after preliminary tests with simulated data showed a higher prediction accuracy, as the initial estimate can be set to the vehicle's known dry mass. A key observation is the faster convergence of the drag coefficients compared to the added mass term. This phenomenon can be explained by the dataset's composition, which contains substantially more data from constant speed segments than from acceleration and deceleration manoeuvrers, the latter being essential for identifying added mass.

Furthermore, it can be observed that the estimated drag along the heading direction exhibits an initial overshoot phase before converging to its final value. This behaviour may be attributed to the LR, which, due to the scheduler, initially induces large variations in the network weights. As a result, the network may temporarily surpass the local minimum towards which the gradient of the optimization function is driving the estimate. However, the purpose of the scheduler is precisely

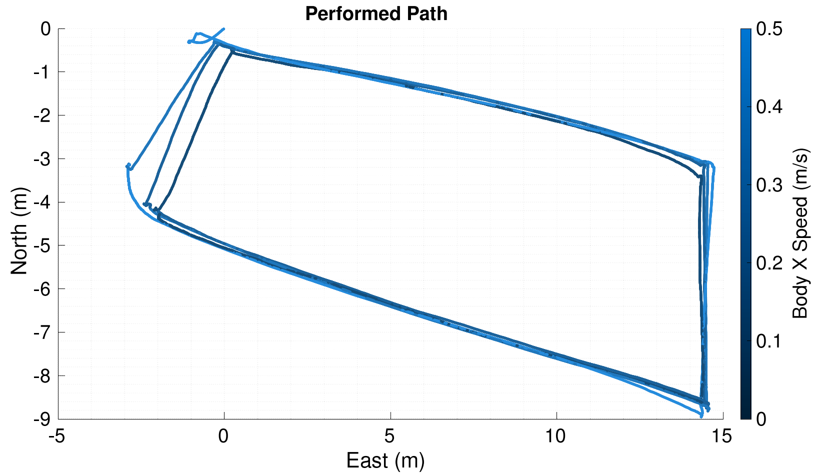

Fig. 6. Path performed to collect identification dataset in survey configuration.

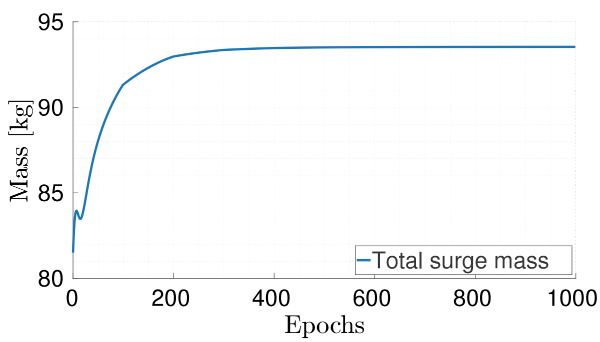

(a)

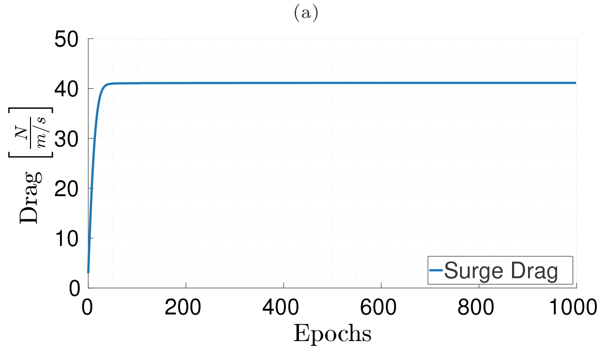

(b)

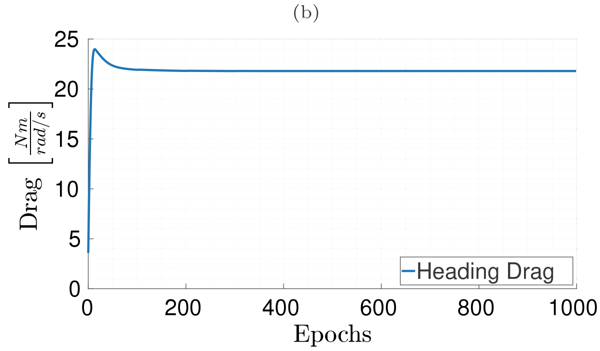

(c)

Fig. 7. Training results for the survey configuration. In (a) the estimation for the added mass. In (b) the results for the drag along surge direction and in (c) the estimation for the drag along heading direction.

Table 3
Estimated parameters for "survey" configuration.

Parameter	Mathematical symbol	Estimated value
Added mass	$X_{\dot{u}}$	24.4 kg
Drag coefficient	D_u	42.13 $\frac{\mathrm{N}}{\mathrm{m/s}}$
Drag coefficient	D_r	21.8 $\frac{\mathrm{Nm}}{\mathrm{rad/s}}$

Table 4
Parameters estimated for "hovering" configuration.

Parameter	Mathematical symbol	Estimated value
Added mass	$X_{\dot{u}}$	39.60 kg
Added mass	$X_{\dot{v}}$	40.41 kg
Drag coefficient	D_u	56.24 $\frac{\mathrm{N}}{\mathrm{m/s}}$
Drag coefficient	D_v	53.05 $\frac{\mathrm{N}}{\mathrm{m/s}}$
Drag coefficient	D_r	26.07 $\frac{\mathrm{Nm}}{\mathrm{rad/s}}$

to progressively reduce the LR as training advances, thereby mitigating the overshoot and promoting convergence towards the correct cost function's minimum.

In particular for the "survey" configuration we have obtained the parameters presented in Table 3.

The second experimental campaign was dedicated to acquiring data for the RUVIFIST vehicle in its "hovering" configuration. Following a similar procedure to the "survey" campaign, the vehicle executed a four-waypoint lawnmower trajectory at multiple speeds (0.4, 0.3, and 0.2 m/s), as depicted in Fig. 8. During this trajectory, the vehicle maintained a near-constant heading to produce sway motion, indicated by red arrows in the figure. To ensure sufficient excitation of all relevant dynamics, a separate, in-place rotation was conducted at the end of the mission to gather data for the yaw DOF.

The mission generated approximately 8000 samples at a frequency of 10 Hz for a total travelled distance of around 200 m. Even in this case the data were processed with the aim of increasing the SNR and obtain better data for the network's training. The training is performed using the same criteria as before, i.e. using a LR scheduler to adjust the LR during the training.

The training results for the estimated parameters, added mass $X_{\dot{u}}$ and $X_{\dot{v}}$, drag D_u and D_v, and drag D_r, are presented in Figs. 9(a) to 9(e). As shown, the estimates converge rapidly, exhibiting large changes in the initial phase of optimization and only minor fluctuations in the final stages.

After all for the "hovering" configuration we have obtained the parameters in Table 4.

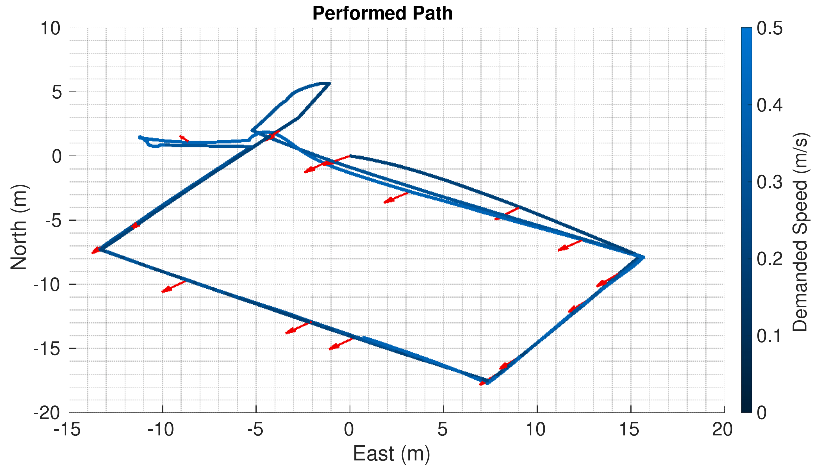

Fig. 8. Path performed to collect identification dataset in hovering configuration. The red arrow on the path shows the vehicle heading during the mission.

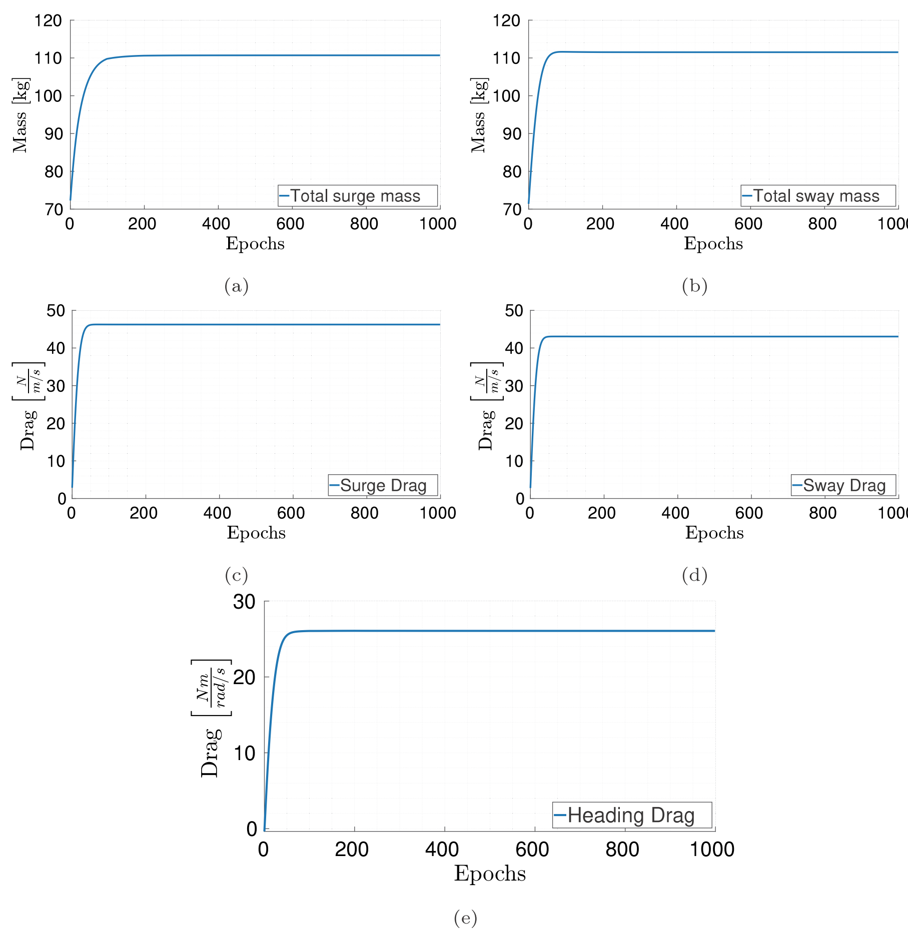

Fig. 9. Training results for the survey configuration. In (a) and (b) the estimation for the added mass for surge and sway configuration respectively. In (c) and (d) the results for the drag along surge and sway direction and lastly in (e) the estimation for the drag along heading direction.

Validation of the estimated parameters

A FF controller, based on the PINN estimations, was implemented to enhance vehicle performance and validate the estimated values. In a first test phase, the FF control action was disabled, and the vehicle was controlled solely by the GS-PID feedback loop. The predicted FF contribution was calculated and logged in real-time to be compared with the GS-PID control action but not provided to the system as control actions. The fidelity of the underlying model was then quantified by comparing this predicted contribution to the actual GS-PID output. In the second phase, the validated FF controller was activated and the system relay only on the FF control action. Fig. 10 shows the validation results for the estimated surge dynamics parameters ($X_{\dot{u}}$ and D_u), obtained while the vehicle follows a straight line to reach a waypoint at a target speed of $0.5\,\mathrm{m/s}$. The bottom plot confirms the goodness of the GS-PID controller, indeed the actual surge velocity (blue) closely tracked the demanded profile (orange), at least at steady state. The top plot demonstrates the model's accuracy, showing strong

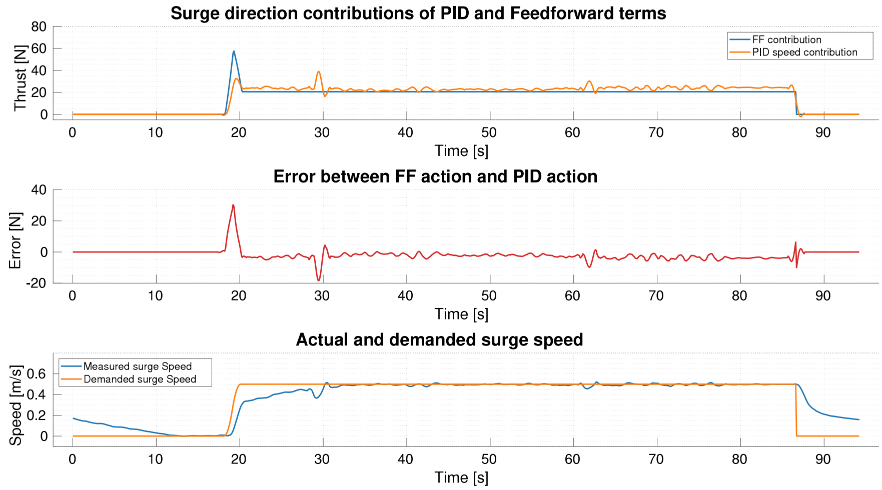

Fig. 10. Surge speed and control action during estimated validation. Top the GS-PID control action and the computed feedforward action with the estimated parameters. Middle the error between the estimated control terms of the FF and the actual control provided by the GS-PID. Bottom present demanded and actual speed of the vehicle along surge direction.

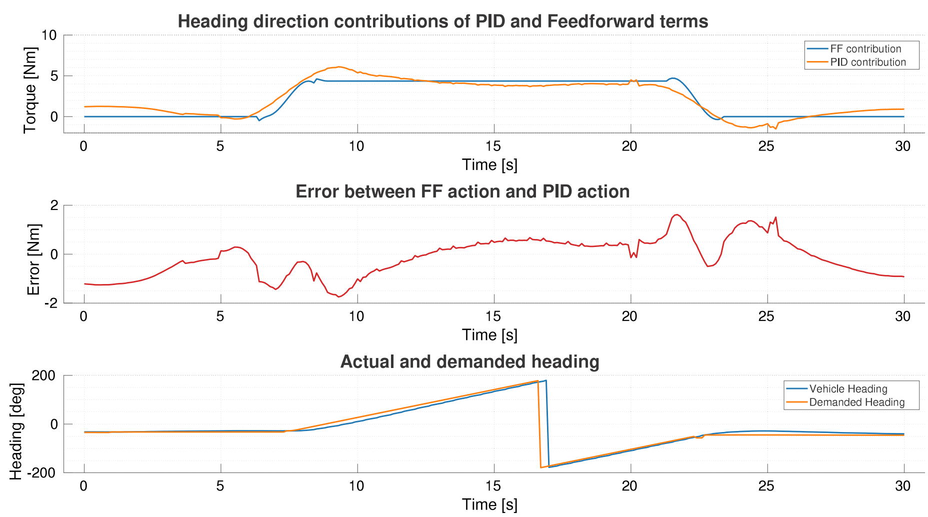

Fig. 11. Results of the test performed to validate the estimation of the rotational drag estimation along heading direction. In the top graph the control action computed by the GS-PID and the FF control system. In the middle graph the error between the control action provided by the computed FF terms and the actual control provided by the GS-PID. In the bottom the heading reference and the actual value measured by the FOG.

correspondence between the FF control action (blue) and the action required by the GS-PID feedback controller (orange), supported also by the middle graph reporting the error between the control action provided by the FF controller and the GS-PID.

At steady state, the GS-PID and FF control actions are nearly identical, with an average error of 2.40 N. The greatest discrepancy occurs during the acceleration phase, where the FF action is higher than that of the GS-PID. This discrepancy is explained by the lower plot, which shows that the GS-PID controller is tuned to be conservative to ensure robustness under various operating conditions.

The same test was performed for the heading DOF of the system and the results are reported in Fig. 11. In this case, the guidance system provided only position references with a linear profile; therefore, the evaluation of the added-mass terms was omitted, as the discontinuities in the reference signal prevented a reliable estimation. In future work, we aim to improve the reference generator to also enable the computation of the second-order derivative of the commanded heading. Fig. 11 shows the results from the on-field validation test for D_r. The highest peak in the error, visible in the middle graph, corresponds to the acceleration phase and is caused by the delay in the system's response.

Since we neglect the added mass along yaw direction, only the phase with constant rotational speed need to be considered. In Fig. 11 the constant speed phase is the one between 7 s to 22 s, i.e. the time interval in which the demanded heading increases linearly. During this phase the control action of the GS-PID and the control action from the FF control system are nearly equal, exposing a mean error of 1.7 N m. In contrast to the surge experiment, the FF control action is lower than the GS-PID's during the transient period. This result is expected, as the term related to angular acceleration is not included in the feedforward model.

Based on the quality of the estimates obtained for the system in the "survey" configuration, we chose not to repeat the same tests for the "hovering" configuration. Instead, we proceeded to the second phase of testing, in which the PID controller was disabled and the system was driven solely by the FF control terms.

Feedforward control action

Since the previous tests revealed discrepancies during the acceleration phase, particularly along the surge direction, and given that

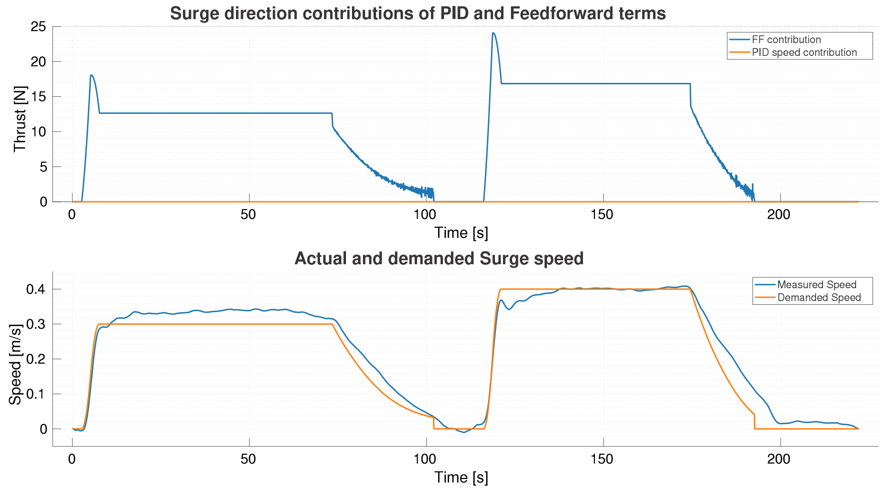

Fig. 12. Evolution of the surge speed for a simple mission with only FF control system enabled.

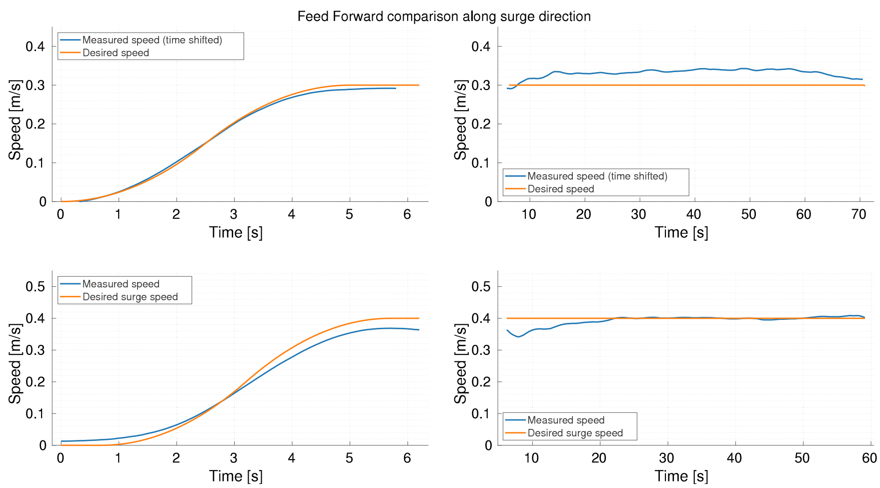

Fig. 13. Acceleration and steady-state comparison in the survey configuration. This figure illustrates an enlarged section of the previous figure, highlighting the two distinct phases: acceleration and steady state.

the acceleration phase governed by the GS-PID controller is highly conservative, additional tests were conducted in both the "survey" and "hovering" configurations. In these tests, only the FF control system was employed to actuate the vehicle. Fig. 12 the results from this second test are presented.

As depicted in the top graph of Fig. 12, the GS-PID feedback controller (orange) was disabled. The bottom panel shows the resulting tracking performance by comparing the desired (orange) and actual (blue) surge velocity. The quantitative analysis focused on two distinct phases. During acceleration, the model demonstrated high accuracy, with a mean tracking error of just $0.0212\,\mathrm{m/s}$. This value was calculated after accounting for the response delay introduced by the physical deadzone of the thrusters. During the subsequent steady-state portion of the trajectory, where performance is governed by the accuracy of the drag estimate, the mean error increased to $0.0336\,\mathrm{m/s}$. Fig. 13 presents the same results as Fig. 12, with an emphasis on the two distinct motion phases: the acceleration phase, in which the added-mass contribution is most significant, and the constant-speed phase, where only the damping terms are presents.

A similar approach was adopted to validate the drag terms along the heading direction, D_r. Even if neglecting the added mass along heading direction does not require a test with only the FF control system to have more information about the goodness of the estimation, an on field test was performed with only the FF terms enabled (Fig. 14).

The dynamic response observed in this test highlights two key deficiencies resulting from the exclusion of added mass in the control model. First, the system's time delay increased greatly. The heading response lagged behind the reference signal by approximately $1.0\,\mathrm{s}$, a sharp contrast to the $0.3\,\mathrm{s}$ delay observed for the surge DOF. Second, the system exhibited significant overshoot. As the vehicle approached the desired heading, the model-based controller underestimated the inertial effects and failed to apply adequate braking torque. Consequently, the vehicle's moment caused it to rotate past the target, leading to a temporary but significant divergence between the commanded and measured heading.

The same test was then performed for the vehicle in "hovering" configuration. Fig. 15 details the validation of the surge dynamics model for the "hovering" configuration using a FF-only test. The results indicate an extremely accurate added mass $X_{\dot{u}}$, evidenced by a minimal mean error of $0.0080\,\mathrm{m/s}$ during the vehicle's acceleration phase. The steady-state performance, related to the linear drag D_u, is also strong; when commanded to a target speed of $0.4\,\mathrm{m/s}$, the system settles at an average speed of $0.3705\,\mathrm{m/s}$, resulting in a mean steady-state error of $0.0295\,\mathrm{m/s}$.

Since in "hovering" configuration also the sway motion is allowed, a dedicated test was performed and the results are shown in Fig. 16. Even in this case the estimation of the dynamics parameters results to be highly accurate for both the added mass $X_{\dot{v}}$ and the drag terms D_v.

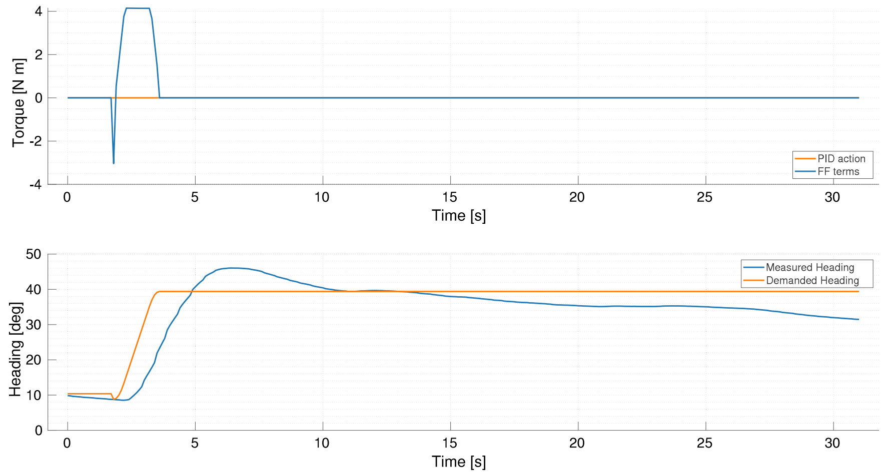

Fig. 14. On field test for heading direction with only FF action enabled. The top graph shows the control action of the PID (blue) and FF control system (orange). In the lower graph the demanded (orange) and measured (blue) heading of the vehicle.

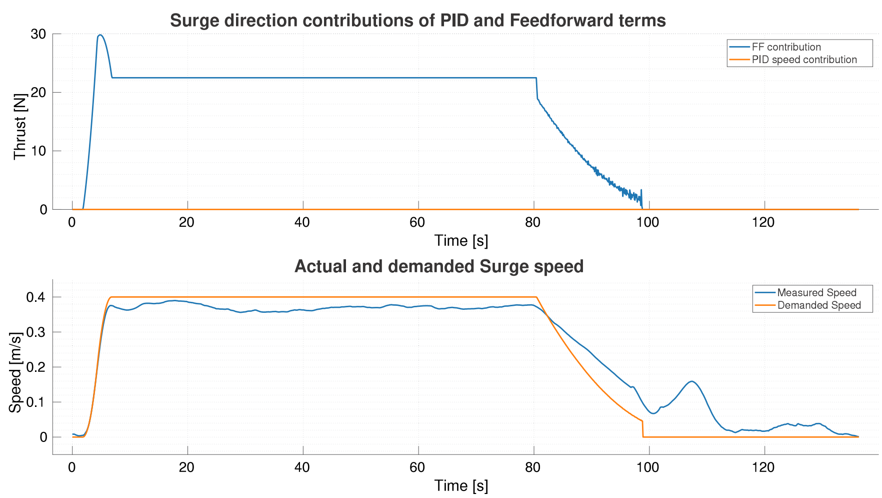

Fig. 15. On field test for surge motion in hovering configuration with only FF action enabled. The top graph shows the control action of the PID (orange) and FF control system (blue). In the lower graph the demanded (orange) and measured (blue) heading of the vehicle.

Indeed for the acceleration phase we have a mean error of $0.0169\,\mathrm{m/s}$ and at the steady state a mean error of $0.0021\,\mathrm{m/s}$.

For the sway motion, the relative accuracy of the two estimated parameters is reversed compared to the surge direction. This can be justified by the imbalance in the training dataset; the data collection path contained longer and more prominent segments of sway motion than surge motion. However, both the surge and sway dynamic parameters results to be sufficiently accurate.

Hybrid control system

Both the configuration employing only the GS-PID controller and that using only the FF controller present limitations. The GS-PID controller exhibits a slow dynamic response, resulting in an extended acceleration phase. The FF control system, on the other hand, is unable to compensate for external or unmodelled disturbances. However, the combination of these two controllers can offer significant advantages, merging the fast response of the FF controller with the disturbance-rejection capability of the GS-PID controller. To show the benefit from combining FF terms and GS-PID control action, a simple test was performed with the vehicle in "hovering" configuration. Fig. 17 shows the results for a surge and sway movement segment with GS-PID and FF control action combined together.

From this experimental analysis, it can be observed that the GS-PID controller generates an average control effort of $-1.1528\,\mathrm{N}$ in the surge direction and $1.6706\,\mathrm{N}$ in the sway direction. The GS-PID control system effects a dual function: it compensates for modelling inaccuracies in the estimated dynamic parameters and simultaneously mitigates the effects of unmodelled external disturbances.

The synergistic combination of the FF and GS-PID control actions yields a significant improvement in the overall tracking performance of the underwater vehicle (Table 5), outperforming either control strategy when applied independently. In particular, compared to the case where only the FF controller is employed (see Figs. 12–15–16), the inclusion of the GS-PID term effectively reduces the delay between the desired and actual velocities, resulting in more accurate and responsive motion tracking.

Comparison between configurations

Beside the improvement in the control system, this estimation procedure allows also to another important results related to the vehicle RUVIFIST. In fact, at the time of writing this thesis, no dynamic analysis

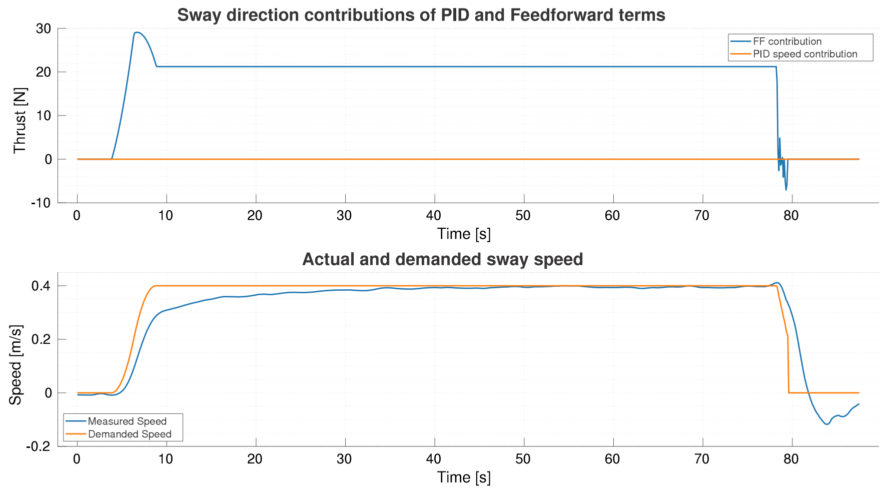

Fig. 16. On field test for sway motion in hovering configuration with only FF action enabled. The top graph shows the control action of the PID (orange) and FF control system (blue). In the lower graph the demanded (orange) and measured (blue) heading of the vehicle.

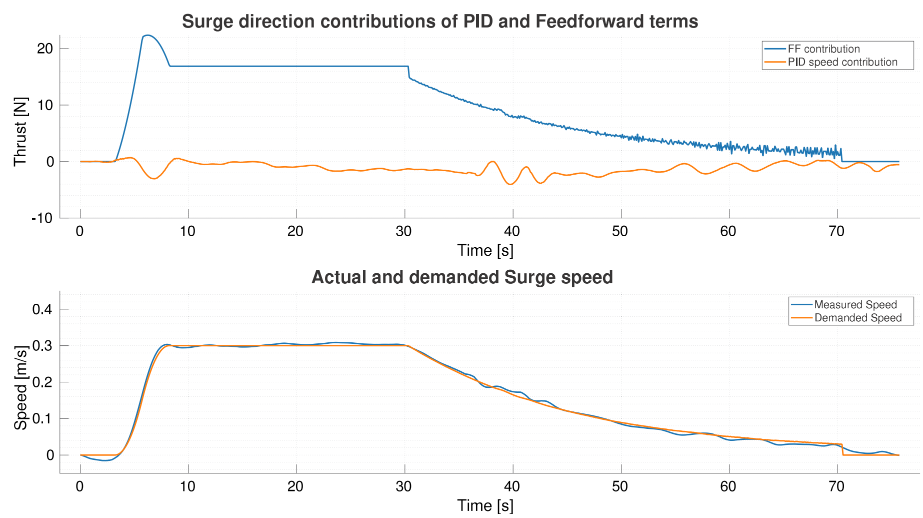

(a)

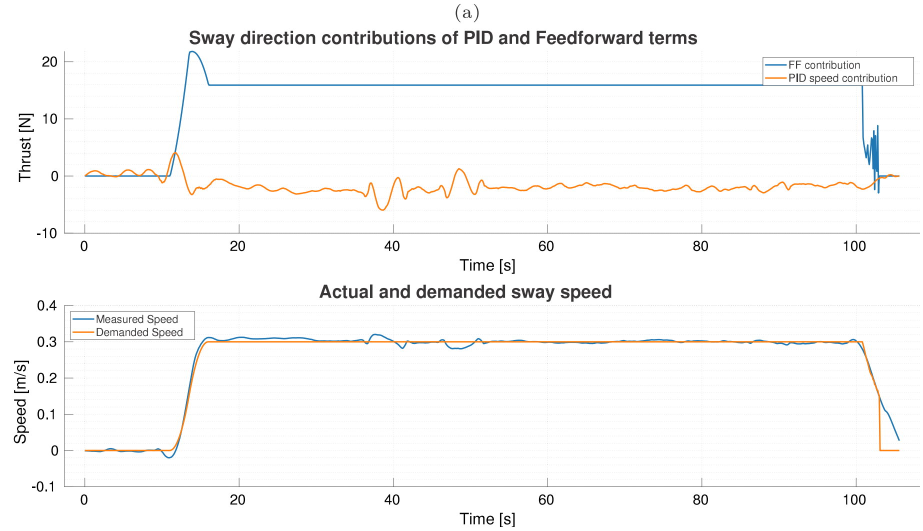

(b)

Fig. 17. Results for surge and sway motion with the combination of GS-PID and FF control actions. In (a) the results for the surge motion, in the top graph control action of the GS-PID (orange) control system and the FF terms (blue) while in the lower graph the desired (orange) and actual (blue) speed. In (b) the results for the sway motion, in the top graph control action of the GS-PID (orange) control system and the FF terms (blue) while in the lower graph the desired (orange) and actual (blue) speed.

Table 5
Tracking error for test with FF and GS-PID control action.

Tracking error	Surge motion	Sway motion
Acceleration	0.0091 m/s	0.0069 m/s
Steady state	0.0036 m/s	0.0030 m/s
Deceleration	0.0048 m/s	0.0026 m/s
Overall	0.0051 m/s	0.0035 m/s

had been carried out on the vehicle to estimate the drag coefficients and added masses of the two configurations. With these estimates, it is now possible to quantify numerically the advantages of one configuration over the other. In particular, by comparing the values in Tables 3 and 4 we can calculate the drag and mass increase between "survey" and "hovering" configuration.

Along the surge direction, the added mass term $D_{\dot{u}}$ increases from 24.40 kg to 39.60 kg, corresponding to a relative increase of 62.30 %. Similarly, the linear drag coefficient D_u rises from 42.13 kg/s to 56.24 kg/s, representing an increase of 33.49 %. This increase in hydrodynamic parameters, combined with the reorientation of the thrusters away from the pure surge axis, results in a substantial increase in the power required for surge motion. Specifically, since the hydrodynamic drag along the surge direction increases by approximately 33 %, the corresponding propulsive force required to maintain a given surge velocity rises by a similar proportion. Furthermore, in the "hovering" configuration, the thrusters are oriented at 34° with respect to the x_{body} axis, so the effective thrust component along the surge direction is reduced. Consequently, the thrusters must generate an even greater total thrust to achieve the same forward force. The combined effect of these two factors leads to an estimated increase of approximately 60 % in the total thrust demand along the surge axis:

$$t_{\text{hovering}} = \frac{1.33}{\cos(0.593412)}\, t_{\text{survey}} = \frac{1.33}{0.82903757255}\, t_{\text{survey}} = 1.604\, t_{\text{survey}} \tag{17}$$

These results are supported by experimental data collected during field campaigns. Indeed, by comparing the power consumption during a transient with $u = 0.2$ m/s in the two configurations, an increase of approximately 55 % is observed.

5. Conclusions and future works

In this study, an innovative neural-network-based identification approach was proposed for estimating the dynamic parameters of a reconfigurable AUV, able to change its shape during an underwater mission. A PINN was developed to infer key parameters, such as added mass and linear damping coefficients, directly from experimental data. By embedding physics-based constraints into the loss function, the model produced physically consistent estimates while reducing the reliance on costly and time-consuming traditional system identification procedures. Experimental validation was central to this work. The results demonstrated that the PINN-based framework achieved high accuracy in parameter estimation. Furthermore, the integration of feed-forward and GS-PID control strategies enhanced system performance, leading to reduced tracking errors. The estimation also enabled a quantitative comparison of survey and hovering configurations, providing new insights into how configuration-dependent added mass and drag effects influence vehicle dynamics. Although the results are promising, the RUVIFIST project presents several avenues for future enhancement. The next step to be addressed is the estimation of the remaining DOFs of the vehicle, in particular the heave direction of motion, and the adaptation of the reference generator along the yaw axis in order to estimate and validate the dynamic parameters related to inertia and added inertia associated with this DOF. After this stage, two different directions can be considered. The first involves increasing the complexity of the dynamic model by including the off-diagonal terms of the mass and damping matrices. The second direction involves the development of more advanced model-based control strategies, such as MPC, exploiting the base system model.

Abbreviations

ARMA AutoRegressive-Moving-Average

AURV Autonomous Underwater Reconfigurable Vehicle

AUV Autonomous Underwater Vehicle

CFD Computational Fluid Dynamics

DL Deep Learning

DNN Deep Neural Network

DOF Degree Of Freedom

DVL Doppler Velocity Log

FC Fully Connected

FF FeedForward

GNSS Global Navigation Satellite System

GS Gain Scheduling

IMU Inertial Measurement Unit

LR Learning Rate

LS Least Squares

LSTM Long Short-Term Memory

ML Machine Learning

MPC Model Predictive Control

MSE Mean Squared Error

NMPC Nonlinear Model Predictive Control

NN Neural Network

PDE Partial Differential Equation

PID Proportional Integral Derivative

PINN Physics-Informed Neural Network

PPC Prescribed Performance Control

ROV Remotely Operated Vehicle

RUVIFIST **R**econfigurable **U**nderwater **V**ehicle for **I**nspection, **F**ree-floating, **I**ntervention and **S**urvey **T**asks

SNR Signal-To-Noise ration

USV Unmanned Surface Vehicle

CRediT authorship contribution statement

Mirco Vangi: Writing – original draft, Software, Methodology, Data curation, Conceptualization. **Alessandro Bucci:** Writing – review & editing, Methodology, Formal analysis, Conceptualization. **Gherardo Liverani:** Writing – review & editing, Software, Resources, Methodology. **Davide Colasanto:** Validation, Data curation. **Alessandro Ridolfi:** Writing – review & editing, Supervision, Project administration, Funding acquisition. **Benedetto Allotta:** Writing – review & editing, Validation, Supervision, Project administration, Funding acquisition.

Declaration of competing interest

The authors declare that they have no known competing financial interests or personal relationships that could have appeared to influence the work reported in this paper.

References

Antonelli, G., Antonelli, G., 2014. Modelling of Underwater Robots. Springer.

Arzani, A., Dawson, S.T., 2021. Data-driven cardiovascular flow modelling: examples and opportunities. J. R. Soc. Interface 18 (175), 20200802.

Bihlo, A., Popovych, R.O., 2022. Physics-informed neural networks for the shallow-water equations on the sphere. J. Comput. Phys. 456, 111024.

Bucci, A., Topini, A., Franchi, M., Zacchini, L., Secciani, N., Ridolfi, A., 2020. Underwater acoustic image enhancement by using fast Super-Resolution with generative adversarial networks. In: Global Oceans 2020: Singapore – U.S. Gulf Coast. pp. 1–8. http://dx.doi.org/10.1109/IEEECONF38699.2020.9389055.

Cai, S., Mao, Z., Wang, Z., Yin, M., Karniadakis, G.E., 2021. Physics-informed neural networks (PINNs) for fluid mechanics: A review. Acta Mech. Sin. 37 (12), 1727–1738.

Chen, G., Wang, W., Dong, J., 2025. Performance-optimize adaptive robust tracking control for USV-UAV heterogeneous systems with uncertainty. IEEE Trans. Veh. Technol. 74 (5), 7251–7262.

Fossen, T.I., 1994. Guidance and Control of Ocean Vehicles. Wiley.

Fossen, T., Sagatun, S., 1991. Adaptive control of nonlinear underwater robotic systems. In: Proceedings. 1991 IEEE International Conference on Robotics and Automation. pp. 1687–1694. http://dx.doi.org/10.1109/ROBOT.1991.131862, vol.2.

Gambarelli, P., Vincenzi, L., et al., 2014. A surrogate-assisted evolutionary algorithm for dynamic structural identification. In: 4th International Conference on Engineering Optimization ENGOPT. pp. 93–98.

Gori, M., Tesi, A., et al., 1992. On the problem of local minima in backpropagation. IEEE Trans. Pattern Anal. Mach. Intell. 14 (1), 76–86.

Gu, W., Primatesta, S., Rizzo, A., 2024. Physics-informed neural network for quadrotor dynamical modeling. Robot. Auton. Syst. 171, 104569. http://dx.doi.org/10.1016/j.robot.2023.104569, URL https://www.sciencedirect.com/science/article/pii/S0921889023002087.

Guzmán, J.L., Hägglund, T., Visioli, A., 2012. Feedforward compensation for PID control loops. In: PID Control in the Third Millennium: Lessons Learned and New Approaches. Springer, pp. 207–234.

Hornik, K., Stinchcombe, M., White, H., 1989. Multilayer feedforward networks are universal approximators. Neural Netw. 2 (5), 359–366.

Kelley, H.J., 1962. Method of gradients. In: Mathematics in Science and Engineering. Vol. 5, Elsevier, pp. 205–254.

Khan, A., Lowther, D.A., 2022. Physics informed neural networks for electromagnetic analysis. IEEE Trans. Magn. 58 (9), 1–4.

Lambert, W., Miller, L., Brizzolara, S., Woolsey, C., 2022. A strip theory and CFD informed lumped parameter model for near-surface underwater vehicle maneuvering. In: OCEANS 2022, Hampton Roads. IEEE, pp. 1–7.

Lee, C.-L., Paulik, M.J., Krishnan, M., 2023. Wheeled mobile robot modeling for local navigation using system identification. In: 2023 IEEE 66th International Midwest Symposium on Circuits and Systems. MWSCAS, IEEE, pp. 394–398.

Liu, J., Borja, P., Della Santina, C., 2024. Physics-Informed neural networks to model and control robots: A theoretical and experimental investigation. Adv. Intell. Syst. 6 (5), 2300385. http://dx.doi.org/10.1002/aisy.202300385, arXiv:https://advanced.onlinelibrary.wiley.com/doi/pdf/10.1002/aisy.202300385 URL https://advanced.onlinelibrary.wiley.com/doi/abs/10.1002/aisy.202300385.

Ljung, L., Forssell, U., 1999. An alternative motivation for the indirect approach to closed-loop identification. IEEE Trans. Autom. Control 44 (11), 2206–2209.

Makam, R., Mane, P., Sundaram, S., Sujit, P., 2023. A comprehensive study on modelling and control of autonomous underwater vehicle. arXiv preprint arXiv:2312.02690.

Martinelli, C., Coraddu, A., Cammarano, A., 2024. Strongly nonlinear multi-degree of freedom systems: Experimental analysis and model identification. Mech. Syst. Signal Process. 218, 111532.

Mishra, S., Makam, R., Sundaram, S., 2024. Data-driven coefficient estimation for autonomous underwater vehicle depth subsystem. In: 2024 IEEE International Conference on Systems, Man, and Cybernetics. SMC, IEEE, pp. 5258–5263.

Nguyen, C., Tran, M., Saji, N., Nguyen, H.D., 2022. Neural network predictive control of explorer class autonomous underwater vehicle. In: 2022 Australian & New Zealand Control Conference. ANZCC, IEEE, pp. 1–6.

Nicodemus, J., Kneifl, J., Fehr, J., Unger, B., 2022. Physics-informed neural networks-based model predictive control for multi-link manipulators. IFAC-PapersOnLine 55 (20), 331–336.

Paszke, A., Gross, S., Massa, F., Lerer, A., Bradbury, J., Chanan, G., Killeen, T., Lin, Z., Gimelshein, N., Antiga, L., et al., 2019. Pytorch: An imperative style, high-performance deep learning library. Adv. Neural Inf. Process. Syst. 32.

Raissi, M., Perdikaris, P., Karniadakis, G.E., 2017. Physics informed deep learning (part i): Data-driven solutions of nonlinear partial differential equations. arXiv preprint arXiv:1711.10561.

Raissi, M., Perdikaris, P., Karniadakis, G.E., 2019. Physics-informed neural networks: A deep learning framework for solving forward and inverse problems involving nonlinear partial differential equations. J. Comput. Phys. 378, 686–707.

Ramirez, W.A., Kocijan, J., Leong, Z.Q., Nguyen, H.D., Jayasinghe, S.G., 2021. Dynamic system identification of underwater vehicles using multi-output Gaussian processes. Int. J. Autom. Comput. 18 (5), 681–693.

Rao Sripada, N., Grant Fisher, D., 1987. Improved least squares identification. Internat. J. Control 46 (6), 1889–1913.

Studt, M., Zhavzharov, I., Abbas, H.S., 2022. Parameter identification and LQR/MPC balancing control of a ballbot. In: 2022 European Control Conference. ECC, IEEE, pp. 1315–1321.

Thothadri, M., Casas, R., Moon, F., D'andrea, R., Johnson Jr., C., 2003. Nonlinear system identification of multi-degree-of-freedom systems. Nonlinear Dynam. 32 (3), 307–322.

Topini, A., Ridolfi, A., 2025. Probabilistic particle filter anchoring (PPFA): A novel perspective in semantic world modeling for autonomous underwater vehicles with acoustic and optical exteroceptive sensors. IEEE J. Ocean. Eng. http://dx.doi.org/10.1109/JOE.2024.3492537.

Van den Hof, P., 1998. Closed-loop issues in system identification. Annu. Rev. Control. 22, 173–186.

Vangi, M., Topini, E., Liverani, G., Topini, A., Ridolfi, A., Allotta, B., 2025. Design, development, and testing of an innovative autonomous underwater reconfigurable vehicle for versatile applications. IEEE J. Ocean. Eng. http://dx.doi.org/10.1109/JOE.2024.3511709.

Vincenzi, L., Gambarelli, P., 2017. A proper infill sampling strategy for improving the speed performance of a surrogate-assisted evolutionary algorithm. Comput. Struct. 178, 58–70.

Visioli, A., 2004. A new design for a PID plus feedforward controller. J. Process Control 14 (4), 457–463.

Visioli, A., 2006. Practical PID Control. Springer.

Xu, P.-F., Han, C.-B., Cheng, H.-X., Cheng, C., Ge, T., 2022. A Physics-Informed neural network for the prediction of unmanned surface vehicle dynamics. J. Mar. Sci. Eng. 10 (2), http://dx.doi.org/10.3390/jmse10020148, URL https://www.mdpi.com/2077-1312/10/2/148.